Received 30 June 2024; revised 29 July 2024; accepted 30 July 2024. Date of publication 6 August 2024; date of current version 20 August 2024.

Digital Object Identifier 10.1109/OJCOMS.2024.3439558

2-Bit RIS Prototyping Enhancing Rapid-Response Space-Time Wavefront Manipulation for Wireless Communication: Experimental Studies

YUFEI ZHAO[1], YUAN FENG[2], AFKAR MOHAMED ISMAIL[1], ZIYUE WANG[1], YONG LIANG GUAN[1] (Senior Member, IEEE), YONGXIN GUO[3] (Fellow, IEEE), AND CHAU YUEN[1] (Fellow, IEEE)

[1]School of Electrical and Electronic Engineering, Nanyang Technological University, Singapore 639798

[2]Department of Electrical and Computer Engineering, National University of Singapore, Singapore 117576

[3]Department of Electrical Engineering, City University of Hong Kong, Hong Kong, SAR, China

CORRESPONDING AUTHOR: Y. FENG (e-mail: y.feng@nus.edu.sg)

This work was supported in part by the National Research Foundation, Singapore, and Infocomm Media Development Authority under its Future Communications Research and Development Programme under Grant FCP-NTU-RG-2022-011 and Grant FCP-NTU-RG-2022-020; in part by MOE Tier 2 under Award MOE-T2EP50220-0019; and in part by the Agency for Science, Technology and Research (A*STAR), Singapore, under Grant M22L1b0110.

ABSTRACT Reconfigurable metasurface, also known as Reconfigurable Intelligent Surfaces (RIS), with its flexible beamforming, low-cost, and easy industrial deployment characteristics, presents many interesting solutions in wireless application scenarios. This paper presents a sophisticated reconfigurable metasurface architecture that introduces an advanced concept of flexible full-array space-time wavefront manipulation with enhanced dynamic capabilities. The practical 2-bit phase-shifting unit cell on the RIS is distinguished by its ability to maintain four stable phase states, each with 90° differences, and features an insertion loss of less than 0.6 dB across a bandwidth of 200 MHz. All reconfigurable unit cells are equipped with meticulously designed control circuits, governed by an intelligent core composed of multiple Micro-Controller Units (MCUs), enabling rapid control response across the entire RIS array. Owing to the capability of each unit cell on the metasurface to independently switch states, the entire RIS is not limited to controlling general beams with specific directional patterns but also generates beams with more complex structures, including multi-focus 3D spot beams and vortex beams. This development substantially broadens its applicability across various industrial wireless transmission scenarios. Moreover, by leveraging the rapid-respond space-time coding and the full-array independent programmability of the RIS prototyping operating at 10.7 GHz, we have demonstrated that: 1) The implementation of 3D spot beams scanning facilitates dynamic beam tracking and real-time communication under the indoor near-field scenario; 2) The rapid wavefront rotation of vortex beams enables precise modulation of signals within the Doppler domain, showcasing an innovative approach to wireless signal manipulation; 3) The beam steering experiments for blocking users under outdoor far-field scenarios, verifying the beamforming capability of the RIS board.

INDEX TERMS Reconfigurable metasurfaces, reconfigurable intelligent surface (RIS), micro-controller unit (MCU), 3D spot beam tracking, vortex beam, rotational Doppler.

I. INTRODUCTION

IN TODAY's urban landscapes, the dense layout of buildings presents substantial obstacles to wireless services, especially affecting vehicles and Unmanned Aerial Vehicles (UAVs) due to potential signal blockages that deteriorate communication quality and may even cause disruptions [1], [2]. Traditional approaches to maintaining consistent connectivity struggle in areas with tall structures,

narrow passages, and various barriers. Recently, reconfigurable metasurfaces, or Reconfigurable Intelligent Surfaces (RISs), have emerged as a viable solution, providing unparalleled control over the propagation of Electro-Magnetic (EM) waves [3], [4]. These surfaces are notable for their adaptable beamforming abilities, affordability, and straightforward integration into industrial settings, marking significant progress in meeting the sophisticated needs of wireless services [5], [6], [7], [8].

While traditional metasurfaces show great promise, their practical use faces several challenges due to complex design and control system limitations, such as fixed states, low-order phase quantization, low response speed, and cumbersome control logic. Previous work has initiated a wave of research into intelligent metasurfaces, such as, [9] and [10] pioneered practical RIS demonstration prototyping in 2020 with limited 1-bit phase modulation capability per unit, which may result in 3 dB energy loss in beamforming caused by the low bit quantization [11], [12]. A year later, [13] unveiled a 2-bit RIS system, which is limited to row-by-row unit control, restricting beam scanning to just one dimension. The design suggested by [14], involving a single Micro-Controller Unit (MCU) and several shift registers, did offer a way to independently control multiple states per unit cell. However, the limited number of I/O ports on the MCU meant that updating all shift registers took too much time, slowing down the RIS's response speed, and limiting its effectiveness in space-time-coding situations.

Drawing inspiration from these remarkable contributions above, we identified the essential need for a RIS system capable of quickly and independently controlling each unit cell without compromising dynamic responsiveness, especially critical in situations requiring fast adaptability. Our research introduces an innovative 2-bit phase-quantized RIS design that enables independent control of each unit while effectively addressing challenges related to space-time dynamic response. This system utilizes multiple MCUs to facilitate swift and efficient state changes, essential for fast beam tracking and space-time coding. Our 2-bit phase-quantized approach and hierarchical control of unit cells significantly improve beamforming capabilities, allowing for the precise and fast adjustment of cone beams and the creation of complex beam structures like spot and vortex beams. This advancement enhances wireless services flexibility and offers solutions tailored to the demanding conditions of modern environments.

Additionally, addressing the complexities of wireless near-field scenarios, we have evolved the traditional 2D beam direction scanning into 3D spatial spot beam scanning and introduced a spot beamforming phase compensation codebook scheme for the phase-quantized RIS. Furthermore, a 3D spot beam tracking algorithm specifically designed for rapidly moving users has been developed. Through feedback between the user and the control system, stable spot beam locking can be achieved, significantly bolstering the RIS prototyping's adaptability to complex EM environments. From theory to practice, innovations at multiple levels in both software and hardware have endowed our RIS prototyping with robust adaptability to various applications. In different experimental scenarios, we demonstrate that (a) 3D spot beam scanning enables dynamic tracking, guaranteeing stable and real-time data transmission with the receiver; (b) vortex beams' space-time wavefront manipulation facilitates precise signal modulation in the Doppler domain, offering a novel signal processing method; (c) beams steering for blocking users under outdoor far-field scenarios, verifying the beamforming capability of the RIS board.

To clarify, the main contributions of this research can be summarized as follows:

1) Firstly, this paper proposes an innovative 2-bit RIS unit cell design through a non-resonant method, that achieves four stable and reconfigurable phase states, while maintaining consistent amplitude attenuation (below 0.6 dB) within the effective bandwidth (over 200 MHz). Incorporating the full-array independent control flexibility, this design furnishes an efficient solution tailored to fulfill the intricate beam steering and space-time-coding requirements.
2) Next, in terms of programmable hardware support, we designed a RIS signal control circuit board consisting of multiple MCUs, enabling *parallel* and *pre-configured* phase states controlling for each independent Radio Frequency (RF) unit cell. The RIS prototyping constructed based on this multi-MCU based hierarchical control system not only achieves highly dynamic beam tracking in horizontal, vertical, and depth (near and far) dimensions, but also enables more complex structured EM waves, e.g., rotational vortex beams. This opens up richer possibilities for future RIS-based wireless transmission solutions.
3) Moreover, this study addresses the characteristics of the EM near-field in multiple reflection scenarios and tailors a spot beamforming codebook scheme for RIS-aided wireless communications, enhancing the precision of 3D spatial beam tracking. A direct and efficient method for implementing spot beam tracking has been proposed in this paper. It introduces a fast spot beam scanning algorithm, facilitating rapid and robust tracking of moving users through comprehensive scans of predetermined spatial regions, which enables stable data transmission within complex reflection interference.
4) Finally, from theory to practice, innovations at multiple levels in both software and hardware have endowed our RIS prototyping with robust adaptability to various applications. It effortlessly handles diverse and complex beamforming requirements, as validated through full-wave EM simulation analyses. In various experimental scenarios, we demonstrated the powerful space-time wavefront manipulation capabilities of the

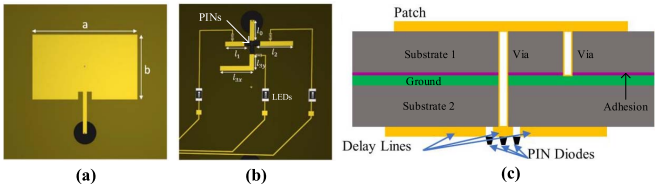

FIGURE 1. Illustrates the innovative design of the RIS unit cell with respect to (a) front-side, (b) back-side, and (c) laminated construction. ($a = 13.8$ mm, $b = 8.3$ mm, $l_0 = 3.46$ mm, $l_1 = 3.84$ mm, $l_2 = 5.64$ mm, $l_3 = 7.64$ mm, width is 0.6 mm for each line).

RIS prototype, providing an efficient testing platform for a wide range of future wireless applications.

The rest of this paper is organized as follows: Section II delves into the 2-bit phase-quantized RIS implementation and its dynamic control system, with a wide comparison of other related works. Section III explains the RIS codebook design, and introduces an efficient 3D spot beam tracking approach, which is verified by the real-time tracking communication experiment. Section IV showcases the vortex wavefront high dynamic manipulation approach, offering a novel signal processing method in the Doppler domain. In Section V, an outdoor far-field test has been implemented to verify the beamforming capability of our RF RIS board. In the end, Section VI concludes this paper and discusses the implications of the findings, potential applications, and avenues for future research.

II. 2-BIT RIS DESIGN WITH ITS POWERFUL CONTROL SYSTEM

A. PHASE-QUANTIZED UNIT CELL

In RIS-aided wireless solutions, the critical aspect for achieving reconfigurability lies in how to design each independent RF discrete unit. Conventional RIS utilizes RF units designed on resonant principles, enabling control of EM wave phase and amplitude through adjustable electronic components that manipulate the equivalent circuit's impedance and reactance to adjust the resonant frequency [15]. However, as the number of reconfigurable states increases, the complexity of the unit cell design escalates [16], [17]. Moreover, nonlinear coupling between different states significantly impacts the independence and stability of state transitions within the unit cell. These problems pose significant challenges for both the design and practical implementation of the whole RIS prototyping [18]. To address these limitations, we introduce a novel non-resonance 2-bit phase-quantized reconfigurable unit cell in this paper, which has been illustrated in Fig. 1. To avoid inter-state coupling effects during state transitions [16], we employ transmission line theory to devise a reconfigurable RF non-resonance structure [19], capable of applying four distinct discrete phase changes to incident EM waves while maintaining consistency in the amplitude.

As shown in Fig. 1, each unit cell consists of three metallic and three dielectric layers. The topmost metallic layer features a rectangular copper patch with dimensions of 13.8 mm $\times$ 8.3 mm. This patch serves as the initial point of engagement with the EM wave, capturing it for further interaction with the other RIS components. Mounted on two 1 mm-thick Taconic TLX-8 dielectric substrates (Substrates 1 and 2). Sandwiched between these substrates is another adhesion layer composed of Rogers RO4450F. Along with the copper ground layer beneath it, which has a thickness of 0.035 mm. A delay line, referred to as l_0, is connected to the patch through a via.

The transmission line lengths in unit cell design are computed based on the principle of achieving specific phase shifts for the reflected signals. The goal is to control the phase of the reflected waves to achieve desired beamforming patterns. The phase shift $\Delta\phi$ introduced by a transmission line of length L is given by $\Delta\phi = \varepsilon L$, where ε is the phase constant of the transmission line, defined as $\varepsilon = 2\pi/\lambda_c$, with λ_c being the wavelength of the operating frequency on the high-frequency laminates. For a 2-bit RIS, we need to achieve four distinct phase states (0, $\pi/2$, π, and $3\pi/2$). The required length L for each phase shift is computed using the following formula,

$$L = \Delta\phi/\varepsilon = \Delta\phi \cdot \lambda_c/2\pi. \tag{1}$$

Specifically, for each phase shift:

$$\begin{cases} L_0 = 0 + \delta, & \text{for } 0 \text{ phase shift,} \\ L_1 = \lambda_c/4 + \delta, & \text{for } \pi/2 \text{ phase shift,} \\ L_2 = \lambda_c/2 + \delta, & \text{for } \pi \text{ phase shift,} \\ L_3 = 3\lambda_c/4 + \delta, & \text{for } 3\pi/2 \text{ phase shift,} \end{cases} \tag{2}$$

where δ is the constant initial length. After the initial design phase, the transmission lines are verified using EM simulation tools such as CST to ensure that the intended phase shifts are accurately achieved. During the physical implementation progress, adjustments are made as necessary to accommodate practical factors such as fabrication tolerances and the properties of the substrate material.

As shown in Fig. 1, the bottom layer of each unit houses three additional delay lines, l_1, l_2, and l_3, with lengths of 3.84 mm, 5.64 mm, and 7.64 mm, respectively. Each of these delay lines is connected to delay line l_0 through individual PIN diodes. These PIN diodes are independently managed by separate signal control lines, each featuring an inductor to isolate Alternating Current (AC) RF signals and mitigate potential interference to the Direct Current (DC) circuit. Additionally, each control line is equipped with an LED to visually indicate the current operational state of the patch. A via grounds the center of the rectangular patch, completing the whole electrical circuit. Engineered to function at a frequency of 10.7 GHz with over 200 MHz bandwidth, the unit cell is capable of four distinct operational states by changing the ON/OFF states of the PINs. The ON/OFF states switching of the PIN diodes forces EM waves to traverse varying lengths of propagation paths within the unit cell structure, thereby imposing different phase delays on

TABLE 1. Comparisons of the reflective RIS prototyping from implementations to applications.

Ref.	Unit cell of the RIS board						Control Circuitry		Functions or
works	Components	Center Freq.	Polar.[a]	States	Ins. loss	Bandwidth	Controller	Control DoF[b]	Applications
[6]	4 PINs	3.5 GHz	LP, CP	2 bit	2 dB	180 MHz	FPGA	By units	Polar. converter
[9]	1 PIN	11.5 GHz	LP	1 bit	1 dB	1 GHz	MCU, FPGA	by units	Beam steerer
[13]	2 PINs	9.5 GHz	LP	2 bit	1 dB	100 MHz	FPGA	By columns	Space-time-coding
[14]	1 PIN	60.25 GHz	LP	1 bit	5.3 dB	450 MHz	FPGA	By units	Beam steerer
[16]	2 PIN	8.0 GHz	LP	2 bit	1 dB	500 MHz	-	By columns	AM PM tunable
[20]	4 PIN	3.6 GHz	LP (daul)	2 bit	<1 dB	400 MHz	FPGA	By rows	Beam steerer
[22]	1 PIN	26.0 GHz	LP	1 bit	<1 dB	400 MHz	FPGA	-	Beam steerer
[23]	5 PIN	2.3 GHz	LP, CP	2 bit, non-	1 dB	400 MHz	FPGA	By units	Beam steerer
[24]	RF Switch	5.3 GHz	LP	3 bit, non-resonant	-	118 MHz	MCU with serial bus	By units	Beam steerer
[25]	1 PIN	28.5 GHz	LP (daul)	1 bit	2 dB	2 GHz	FPGA	By units	Beam steerer
[26]	1 PIN	27.5 GHz	LP	1 bit	<3 dB	5.25 GHz	-	By units	Beam steerer
[27]	1 Varactor	3.6 GHz	LP	2 bit	1.2 dB	<400 MHz	FPGA	By columns	Time-digi.-coding
[28]	4 Varactors	3.7 GHz	LP	Multi-bit	<3 dB	-	FPGA	By columns	Time-digi.-coding
This work	3 PINs	10.7 GHz	LP	2 bit, non-resonant	0.6 dB	200 MHz	Hierarchical MCUs	By units	Spot beam steerer, rotational vortex

[a] LP: Linear polarization; CP: Circular polarization. [b] DoF: Degree of freedom. It indicates the degree of flexibility with which the entire RIS array can be controlled. It depends on the specific applications of each RIS prototyping.

the reflected signal. We simulate the unit cell together with PIN diodes SMP1320 under CST Studio Suite environment, and the results have been shown in Fig. 2. Obviously, the amplitude attenuations of the reflected signal of the four states of each unit remain below 0.6 dB within a 200 MHz bandwidth (10.6 $\sim$ 10.8 GHz), while the phase differences are stabilized at about 90° among them. It is worth noting that for a 2-bit RIS design, achieving amplitude attenuation within 1 dB is already considered outstanding performance [13], [20], [21].

As we know, in recent years, research on RIS has flourished. To better showcase the works of various researchers on reflective RIS prototypes over the past few years, a comparative Table 1 has been created that lists the key features of our proposed design alongside those of existing works. As shown in Table 1, current RIS prototype research varies significantly, primarily due to specialized designs aimed at different application scenarios. There is no standardized design scheme at present. To match actual application scenarios, RIS prototypes focus not only on hardware metasurface design but also on comprehensive system engineering, which includes selecting control chips, circuit design, software algorithms, and communication protocols among various components. For instance, the project in [22] demonstrates an RIS-enabled ultra-massive MIMO system in a practical test-bed and addresses practical challenges

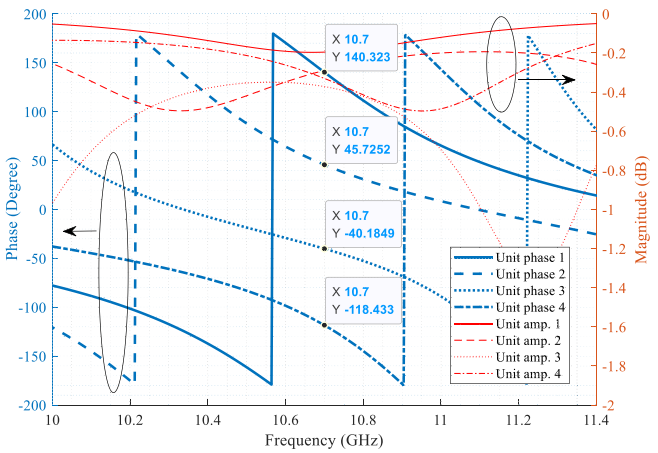

FIGURE 2. Phase and amplitude simulations of the 2-bit unit cell.

by integrating commercial NR base stations and off-the-shelf user equipment. In [23], Dai et al. also successfully achieve 2-bit phase shifting using non-resonant unit cells, which contributes to the industrialization of RIS prototyping. Then, in [24], Rossanese et al. proposed another non-resonant RIS unit cell design based on the RF switch. The researchers in [25] and [26] explore azimuth and elevation beam control with independent control mechanisms and 1-bit

reconfigurable unit cells. Moreover, References [27] and [28] initially introduced the time-domain digital-coding concept for metasurfaces, which significantly enhanced the flexibility of RIS prototypes and opened up a new research area for future RIS applications.

Inspired by previous research, in this work, we are dedicated to introducing a novel design concept for the RIS prototype. Firstly, We propose a more straightforward unit cell design through the non-resonant principle to achieve 2-bit phase shifting. In our design, different phase shifts correspond to distinct delay line paths that are independent of each other. When a PIN diode switches to select a different path, it does not affect the other paths, thereby minimizing the interaction between different phase states. The switching speed of the PIN diodes is typically in the nanosecond range, which is sufficient to ensure rapid transitions between phase states. It is worth noting that this approach avoids the repeated adjustments of the equivalent circuit resonance states of unit cells required by many existing works, significantly simplifying the RIS unit cell design process.

Secondly, as shown in Table 1, numerous studies have managed to achieve multi-bit state reconfigurability for RIS. However, to transition RIS from a laboratory setting to commercial use, the control of RIS should not be overlooked. Developing a mechanism to achieve more flexible and rapid dynamic responses, enabling the RIS prototype to adapt to more complex application scenarios, remains a challenging issue. Hence, the following sections of this paper introduce a hierarchical control mechanism based on parallel processing and pre-configuration. The control architecture employs multiple MCUs, each equipped with its own storage and computational capabilities. Each follower MCU is responsible for controlling a small subset of RIS unit cells and operates under the directives of a leader MCU. Unlike simple registers, each MCU in our control board has independent storage and computational resources, enabling it to pre-configure various codebook states for the unit cells under its control. Upon receiving instructions from the leader MCU, each follower MCU can rapidly switch states, which significantly accelerates the transition process.

Furthermore, in our design, each unit cell of the RIS can independently change its response state under the control system, allowing for functionalities such as rapid beam steering, near-field spot beam tracking, and vortex wavefront rotational modulation. All these features will be sequentially demonstrated in the following sections. Additionally, thanks to its flexible space-time digital coding ability, our system can quickly achieve continuous rotational speed shifts of complex vortex beam wavefront. This capability enables the receiver to observe the effects of carrier Doppler frequency shifts in the frequency domain. These are the distinctive features that set the RIS prototyping and the design methodology proposed in this paper apart from previous works.

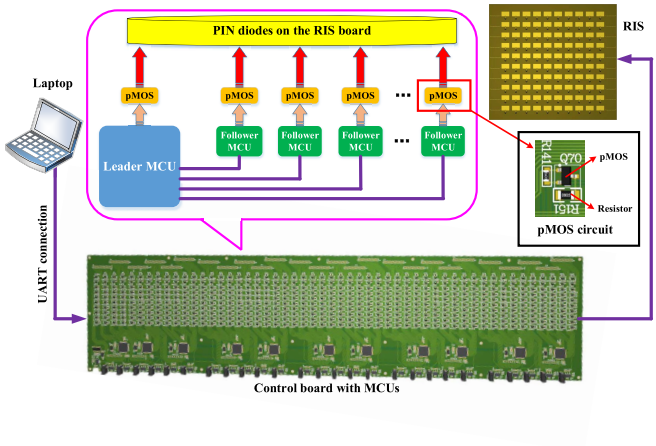

FIGURE 3. Demonstrating the connection relationship and signal transmitting progress of the whole RIS system with control circuitry.

B. RAPIDLY-RESPOND CONTROL CIRCUITRY WITH MULTI-MCU

Specifically, the current RIS prototyping contains 10×10 RF units with an amount of 300 PIN diodes, which are connected to a user-defined core signal control board employing multi-MCU chips on it [14]. The dynamic reconfigurable functionality relies on a meticulously designed control board, employing 11 MSP430F5529 MCUs, where one serves as a leader MCU and the remaining 10 functions as follower MCUs. This configuration exemplifies distributed processing, facilitating efficient control of the whole RIS system. As demonstrated in Fig. 3, a total of 520 output pins are formed by soldering the Metal-Oxide-Semiconductor Field Effect Transistor (MOSFET) circuit to each General Purpose Input/Output (GPIO) pin of the MCUs. Specifically, the leader MCU has 20 GPIOs left available for controlling the PIN diodes, and each of the 10 follower MCUs has 50 GPIOs available for use. This arrangement provides 520 output pins, creating a sophisticated control mechanism that can handle a multitude of patterns. The MOSFET circuit, consisting of 1 p-channel-MOS (pMOS) and 2 resistors, is triggered on negative voltage values, which inversion of input-output logic, wherein '0' represents 0V and '1' represents 3.3V, increases the robustness of the control circuit. While the control board possesses 520 output pins, only 300 are used, connecting to the current RIS board's control lines. (Actually, we over-design the control circuitry for other potential functions in the future. As the level of industrial completion improves, the whole control system will also become more compact and lightweight.)

Suppose that a codebook $\mathbf{U}^{10\times10} \in \{0, 1, 2, 3\}$ can be used to represent the state of each unit cell on the RIS board. Four numbers represent four quantized phase states. Each unit cell is controlled by three PIN diodes, with different ON/OFF state combinations governing the 2-bit phase transition switch. Hence, from this codebook, the binary state of each of the 300 pins can be determined.

Binary data is then converted to hexadecimal data, ready to be transmitted to the MCUs. The leader MCU, upon power-up, establishes a connection with a PC via USB, employing a Universal Asynchronous Receiver/Transmitter (UART) for data transmission. The MCUs will receive control instructions together with the codebooks of the RIS phase patterns from the PC. The leader MCU validates the receiving data, extracts relevant information, and prepares it for each follower MCU. The data transmission protocol used is Serial Peripheral Interface (SPI), promoting high-speed data exchange between the leader and follower MCU. Moreover, for the control system, the codebooks are pre-loaded into the leader MCU, which is connected to the other follower MCUs via SPI. Each follower MCU independently controls a small subset of PIN diodes' ON/OFF states. Upon receiving commands, all follower MCUs can operate in parallel without interfering with each other. This parallel processing and pre-configuration mechanism significantly enhances the operational efficiency of the RIS control system, thus increasing the refresh rate of the entire RIS array.

For instance, the follower MCUs have 9 output ports connected to the RIS PIN diodes, with each port's data size being 8 bits (1 byte). Assuming that command data is sent from the leader MCU to the other 10 followers within one clock signal, and each follower receives 9 bytes of data, the total time taken for SPI communication is calculated based on the number of bits sent and the baud rate (in bits per second). Therefore, for 10 followers, 9 bytes per follower, and a baud rate of 1 Mbps, the total action time for SPI communication can be calculated as $10 \times 9 \times 8\,\text{bits}/1\,\text{Mbps} = 0.72$ ms. In other words, the control system needs at least 0.72 ms to switch to a phase distribution corresponding to a new codebook, i.e., $D_t = 0.72$ ms which will be described in Section III. Assuming we divide the half-space served by the RIS into $P = 20$ regions of different sizes, and $t_d = 1$ ms, then the time required for the RIS to traverse all codebooks is approximately 15.4 ms for our current hardware design. Indeed, the RIS prototyping proposed in this paper is still in the initial stages of development, and many signal processing algorithms are not fully embedded in the MCUs but are instead executed using LabVIEW and MATLAB, which leads to noticeable delays in the demos. As the level of industrial completion improves, the speed of time-domain coding processing in this RIS prototyping, which has parallel processing and pre-configuration capabilities, will undoubtedly accelerate.

C. SIMULATION, FABRICATION AND MEASUREMENT

After fabrication and assembly, the entirety of the RIS along with its control system is depicted in Fig. 4. The RIS panel itself measures 228 mm by 208 mm and comprises 100 unit cells arranged in a 10 × 10 grid, in addition to 20 plug headers that serve to connect the control lines of each unit cell to the pMOS circuit on the control board. When there is a change in the phase state of the RIS, LEDs positioned on the backside flash in accordance with the ON/OFF status of the PIN diodes, offering a direct method to monitor the operational state of the entire RIS prototyping visually.

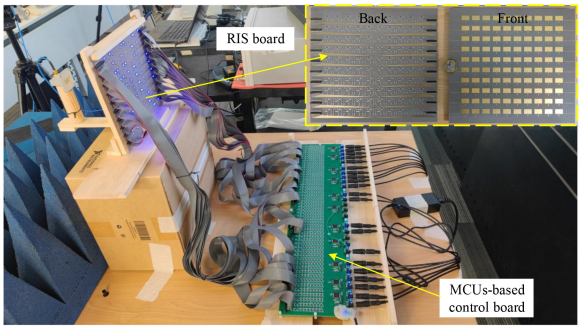

FIGURE 4. Fabrication of the RIS prototyping.

As we know, mutual coupling arises from the EM interaction between closely spaced unit cells, leading to induced currents that affect the current distribution on each unit cell. The altered current distribution due to mutual coupling can result in phase errors and amplitude variations across the array, which negatively impact beamforming. Increasing the spacing between unit cells can significantly reduce coupling effects, but excessively large spacing can lead to higher side lobes in the radiation pattern due to spatial under-sampling. In our design, we carefully chose the unit-cell size to be approximately 3/5 of a wavelength. This dimension is optimized through CST under periodic boundary conditions. The slightly larger spacing helps to mitigate mutual coupling without significantly affecting the beamforming performance. For the inter-state coupling, our design utilizes microstrip transmission lines of varying lengths to achieve phase shifts. The reconfigurable phase state of each unit cell is directly correlated with the physical length of each transmission line, which minimizes inter-state coupling by ensuring that each phase state corresponds to a unique and independent transmission path.

Furthermore, the simulations were designed to verify the beamforming capabilities of the RIS prototyping. As illustrated in Fig. 5(a), the beam emanating from the transmitter, once modulated by the RIS, creates two energy-dense regions. These regions materialize concurrently in front of the RIS normal with different locations, demonstrating the RIS's ability to serve two distinct users simultaneously without spatial interference. This scenario, depicted as a representative example calculated via MATLAB, showcases the potential for generating multiple spot beamformings through the RIS by employing various codebooks, further exemplified in Fig. 5(b) and Fig. 5(c). In Fig. 5(b), the two spot beams are positioned on either side of the RIS's normal, while in Fig. 5(c), the spot beams materialize at asymmetric locations in space, predetermined by the system's configuration. This versatility in beam placement underscores the RIS's advanced beamforming potential, enabling precise and flexible targeting to meet diverse wireless applications,

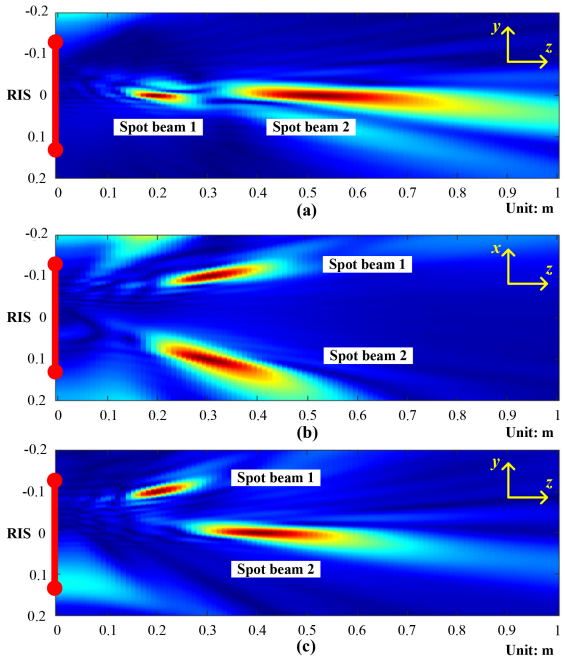

FIGURE 5. Simulation results for the 3D spot beamforming. (a) 2 spot beams along the normal direction of the RIS. (b) 2 spot beams located on either side of the RIS normal direction. (c) 2 spot beams positioned at asymmetric locations in the near field of the RIS.

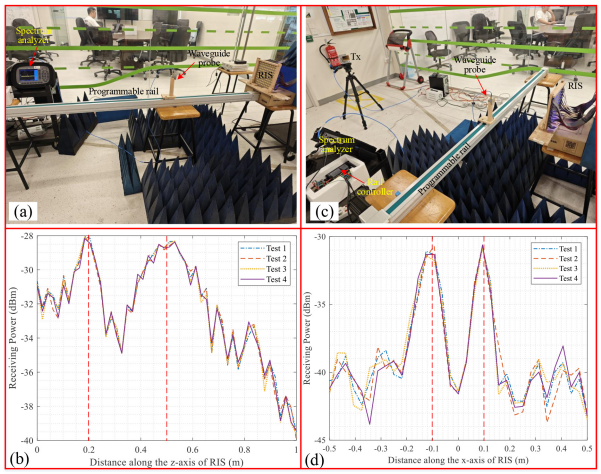

FIGURE 6. Measurement for the 3D spot beamforming. (a) Measurement along the *z*-axis perpendicular to the RIS plane. (b) Energy distribution along the *z*-axis, results from (a). (c) Measurement along the *x*-axis parallel to the RIS plane. (b) Energy distribution along the *x*-axis (0.3 m apart), results from (c). (The red vertical lines indicate the measured positions of the peak power).

e.g., multi-focus wireless power transfer, wireless sensor networks, and device-to-device communications.

Additionally, a measurement experiment is set up to replicate the spot beamforming results observed in the above simulations. As shown in Fig. 6, we positioned a rail in front of the RIS. On the rail, there is a slider that can move step-by-step along the rail according to the programming. A waveguide probe mounted on the slider is connected to a spectrum analyzer to measure and record the spatial EM signal energy at each location. The experimental setup is designed to validate the simulation results shown in Fig. 5(a) and Fig. 5(b), corresponding to two spot beamforming schemes, i.e., one perpendicular to the RIS plane and the other parallel to the RIS plane. In the measurement, the same RIS phase distribution pattern was programmed into the MCUs-based control board. As illustrated in Fig. 6(a), the linear rail was aligned perpendicular to the RIS plane, and the waveguide probe traversed from near to far along the rail, with the spectrum analyzer capturing the spatial energy distribution. The corresponding measurements, presented in Fig. 6(b), consistently revealed two prominent energy peaks at distances of approximately 0.2m and 0.5m from the RIS plane, demonstrating focused beam energy at these points, which is consistent with the simulation results in Fig. 5(a). Similarly, to validate Fig. 5(b), the linear rail was set parallel to the RIS plane at a distance of about 0.3m, and the waveguide probe was programmed to traverse from right to left. The spectrum analyzer systematically recorded the energy distribution along this path, as depicted in Fig. 6(c). The findings, summarized in Fig. 6(d), displayed consistent dual energy peaks flanking the normal to the center of the RIS, confirming the simulation results in Fig. 5(b).

Furthermore, it is worth noting that for some reconfigurable metasurface schemes, although each unit cell has the capability of 2-bit phase states control, only the entire row or column of unit states can be adjusted simultaneously due to limitations in the control system [29]. Such RIS typically only possesses the ability for cone beamforming and cannot form spot beams, let alone structured EM waves such as vortex beams. Structured EM waves, characterized by the intricate phase structure within the beam, typically necessitate RIS to have at least simultaneous 2D control capabilities for generation. In this paper, the proposed RIS prototyping allows each unit cell to be independently controlled, with less coupling between different reconfigurable phase states. Fig. 7(a)(b) display two types of full-wave simulation results generating vortex beams in the CST environment, further demonstrating the flexible beamforming capabilities of the proposed RIS prototyping. These results not only highlight the advanced functionality but also its potential to significantly impact the development of many wireless solutions by facilitating more complex and efficient signal distribution strategies, which will be demonstrated in our experiments.

III. RIS-BASED SPOT BEAMFORMING AND TRACKING SCHEME FOR RAPIDLY-RESPOND SOLUTIONS

A. CODEBOOK DESIGN FOR RIS SPOT BEAMFORMING

In general, we consider $2D^2/\lambda$ as the boundary distinguishing between the far-field and near-field of the RF transmitter, where D denotes the aperture size of the radiator, λ is the wavelength. However, in the RIS-assisted urban wireless communication environment, with the increase in the 2D aperture size of the RIS board and the higher carrier

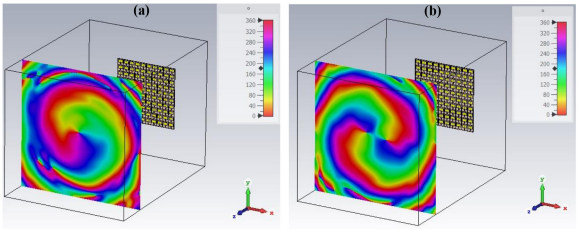

FIGURE 7. Generation for vortex beams under CST Studio Suite. (a) Vortex topology mode 1. (b) Vortex topology mode 2.

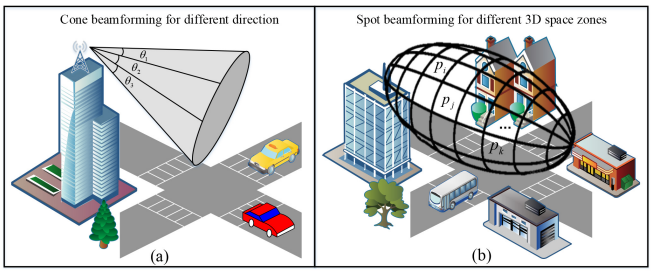

FIGURE 8. 2D directional beamforming vs. 3D spot beamforming.

frequencies, the assumption of ideal far-field communication conditions no longer holds in practical scenarios [30], [31]. This influence is particularly evident in the beam-steering aspect of the antenna array. As shown in Fig. 8(a), under the traditional far-field assumptions, the beams controlled by the transmitter are cone-shaped beams, i.e., the receiving users are at specific angular directions of the transmitter. In some specific scenarios, such as serving far-field users with a 2D directional beamforming requirement, the unit cells distributed in a particular column or row on the RIS might exhibit an approximately identical phase distribution. This could simplify the control circuit of the RIS. Nonetheless, for comprehensive beam steering at both azimuth and elevation angles, the phase profile requires individual configuration of each unit cell, which also demands a more complex control mechanism [25], [26]. Generally, in real-world applications, especially in congested urban environments, both the transmitter and receiver are in the near-field region of the metasurface [32]. In 2023, Sadeghian et al. discusses the impact of RIS in indoor environments and suggests that a significantly large RIS might be necessary to make a noticeable difference compared to ambient propagation [33]. In this scenario, what is incident on the RIS board is no longer a planar wave but a spherical wavefront with a structured phase. As demonstrated in Fig. 8(b), beamforming is affected not only by the angular dimension but also by the distance. It has evolved from traditional 2D beam scanning to 3D spatial beam focusing. In this context, distinct from traditional cone beamforming, the new RIS-based codebook design can be referred to as spot beamforming.

In the Cartesian coordinate system, assume that the center of the RIS is the coordinate origin, the coordinates of each unit cell on the RIS board can be represented by $\mathbf{u}_{m,n} = (x_{m,n}, y_{m,n}, z_{m,n})$, $m \in \{1, 2, \ldots, M\}$, $n \in \{1, 2, \ldots, N\}$, $M \times N$ is the total number of the discrete unit cells on the RIS board, and the transmitter's coordinates relative to the RIS are denoted as $\mathbf{u}_{\mathrm{T}} = (x_{\mathrm{T}}, y_{\mathrm{T}}, z_{\mathrm{T}})$. Then, the half-space served by the RIS can be partitioned into P distinct receiving regions based on varying angles and distances. We can assume the coordinates of the center of each receiving region as $\mathbf{p}_i = (x_i, y_i, z_i)$, $i = 1, \ldots, P$. Evidently, the number of codebooks recorded by the RIS is directly associated with the granularity of spatial partitioning. Each codebook essentially corresponds to a 2-bit quantized phase distribution state on the RIS board.

Without loss of generality, assume that the RIS is placed at the x-y plane. Generally, the positions of the transmitter and RIS are relatively fixed. Based on pre-defined coordinate positions, it is straightforward to calculate the geometric distance from the transmitter to each unit on the RIS as,

$$d_{m,n} = \sqrt{\left(x_{\mathrm{T}} - x_{m,n}\right)^2 + \left(y_{\mathrm{T}} - y_{m,n}\right)^2 + \left(z_{\mathrm{T}} - z_{m,n}\right)^2}. \quad (3)$$

Then, the electric field reaching the m-th row and n-th column of the RIS can be calculated as,

$$\vec{E}(m, n) = \frac{G\lambda}{4\pi d_{m,n}} \exp\left(-jkd_{m,n}\right), \quad (4)$$

where G is the propagation constant associated with physical factors such as antenna gain and radiation pattern, $k = 2\pi/\lambda$ is the wave vector, j is the imaginary unit. According to the principle of wave interference, after reflection from all units on the RIS, the EM waves reaching a specific spatial grid should coherently superimpose with the same phase [34]. Let's simplify by considering the center point of the grid as the reference for beam interference. In this case, the propagation path difference from distinct units to the reference point can be calculated as,

$$f_{m,n,i} = \sqrt{\left(x_{m,n} - x_i\right)^2 + \left(y_{m,n} - y_i\right)^2 + \left(z_i - z_{m,n}\right)^2} - z_i. \quad (5)$$

If we view the propagation of EM waves as a series of rays, in order to compensate for the phase differences introduced by the spatial positions of distinct unit cells during the propagation process, for each unit cell, the required interference compensation phase offset can be got from the following equation,

$$T_{m,n,i} = \frac{(4\pi)^2 d_{m,n} d_{m,n,i}}{G\lambda^2} \exp\left(jkd_{m,n} + jkf_{m,n,i}\right), \quad (6)$$

where, $d_{m,n,i} = |\mathbf{u}_{m,n} - \mathbf{p}_i|$. If the RIS simultaneously serves multiple users in different spatial grids, then the compensation on each unit cell is the vector sum of the calculated results from (6), i.e.,

$$T_{m,n} = \underset{2\text{ - bit}}{\mathrm{quantize}}\left\{\mathrm{angle}\left[\sum_{i=1}^{P} T_{m,n,i}\right]\right\}, \quad (7)$$

where $\underset{2\text{ - bit}}{\mathrm{quantize}}\{*\}$ represents the phase bit quantization operation, which needs to be determined based on the actual

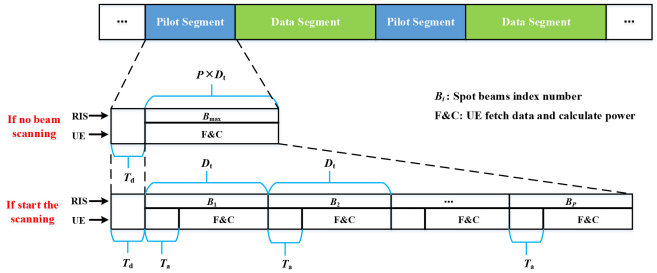

FIGURE 9. Signal frame structure and timeline for beam scanning.

full wave phase simulation results of the unit cells. $T_{m,n}$ is one codebook of the 3D spot beams on the RIS. Before applying the beam tracking algorithm, all codebooks will be pre-loaded into the MCU controlling the RIS board.

B. RIS-BASED SWIFT BEAM TRACKING SCHEME

In this part, we introduce a beam scanning approach aimed at tracking moving users and sustaining ongoing communication in intricate near-field settings. Spot beam scanning is a method where the RIS sequentially forms beams across each pre-defined 3D spatial region within its coverage half-space. The sequencing of the beam scanning is depicted in Fig. 9. This process is primarily conducted during the pilot phase, where beams with varied shapes are dispatched in a time-division fashion. Every 3D spatial region is associated with a distinct scanning time slot, with the procedure repeating until the complete half-space has been covered.

The specific process of dynamic beam tracking of the mobile user based on RIS is as follows:

- First, set the spatial coordinates between the transmitter and RIS, dividing the RIS's coverage into P zones. The transmitter sends signals as shown in Fig. 9. After RIS beamforming, users demodulate the signal, calculating the receiving power p_r. Users set a reception power threshold g_t, based on their sensitivity. If the signal power drops below this threshold, they inform the RIS to start beam scanning.
- Next, for precise beam scanning, synchronization between the user and RIS on the scanning start time is crucial. Upon requesting a scan, the user also sends its local time to the RIS. The user checks its time T_u and accounts for transmission and processing delays t_d, ensuring the delay τ, from when the RIS starts scanning T_s to the user's time, exceeds the delay time T_d. Accurate time synchronization is vital and can be achieved using the Network Time Protocol (NTP), which synchronizes devices with time sources to ms accuracy [35].
- Then, at the predetermined time T_s, the RIS begins to direct spot beams to the designated spatial regions, setting each beam's duration to D_t. This duration, ideally, is the time needed for the RIS to adjust the reflection coefficients for its array. Starting T_a ms after T_s, the user samples data, measures its power, and logs this as the reception power for that region. To ensure data capture and power calculation align with the current beam's duration, T_a must be less than D_t. The user then repeats this process every D_t ms, guaranteeing that measurements for each region are taken within their respective beam durations.
- After scanning each pre-defined spatial region, the user identifies the receiving power for regions targeted by the converged spot beam. By comparing these values, the user selects the beam with the highest receiving power and informs the RIS of the selected beam ID B_{ID}. The RIS then adjusts the reflection coefficients across its array to form the beam shape corresponding to B_{ID}, completing the dynamic beam tracking process. The total scanning duration is influenced by the delay T_d from transmission and processing, plus the cumulative scanning time for all receiving regions, i.e.,

$$t_{tot} = T_d + P \times D_t, \tag{8}$$

P RIS patterns equal to P spatial receiving regions.

To clarify, the steps of the RIS-based dynamic 3D beam tracking algorithm are listed as Algorithm 1.

This algorithm can be easily adapted to various RIS prototypes as a direct and efficient method for implementing spot beam tracking, without concern for frequency, bit quantization, or even partial components failure. The beam shapes for different 3D regions are pre-configured into the

Algorithm 1 RIS-Based 3D Spot Beam Dynamic Tracking

INPUT: Receiving power p_r, sensitivity threshold g_t, user's local system time T_u, duration time D_t for each spot beam, delay T_a.
  While(1) *% keep monitoring the receiving power* p_r *and do sweeping if need*
    If($p_r < g_t$)
      UE Check the local system time T_u;
      Determine the time T_s to start the beam scanning, where, $T_s = T_u + T_d$;
      Then do the feedback and transmit T_s from the user to the RIS;
      Do spot beams scanning on the RIS, while calculating the receiving power on the user;
      For($B_{ID} = 0; B_{ID} = P; B_{ID}++$)
        Delay T_a ms;
        Fetch signal and calculate power on the user side, and recorded as u_r;
        Delay $D_t - T_a$ ms;
      End For
      Compare and find the largest u_r, recorded as p_r;
      $B_{max} = \max \text{index}(p_r)$; *% Find the beam index* B_{max} *of the largest receiving power ar the UE side*
      Do the feedback of B_{max}, from user to RIS;
      Then RIS change to the B_{max}-th pattern;
  End While

MCUs of the RIS prototyping, and the feedback mechanism is based on basic power threshold detection. This means that, in practical applications, there is no need for extensive pre-mapping or concern about random reflections affecting the codebook shapes. It can always find a codebook shape through scanning and achieve quick feedback and state locking (Although the codebook may not be optimal, it definitely ensures that the spatial beam exceeds the detection threshold at the receiver at that moment), enabling true plug-and-play functionality for the RIS system. The implementation cost of this mechanism involves pre-configuration of the 3D space codebooks and achieving fast switching between them. It should be noted that, in the scanning feedback process, we introduced a feedback principle based on exceeding detection thresholds rather than waiting for all codebooks to be scanned and then taking the maximum value. This significantly improves scanning efficiency and differs from traditional codebook-based schemes. Considering the inherent error correction mechanisms in communication systems, maintaining a certain detection power threshold ensures stable data transmission. This robustness is demonstrated in the following experiments, where stable tracking is achieved even with environmental disturbances.

C. RIS-BASED REAL-TIME TRACKING AND COMMUNICATION EXPERIMENTS FOR MOVING USER WITH 3D SPOT BEAMS

To verify the above algorithm, a real-time tracking and communication experiment based on RIS for the moving user has been set up in a complex environment filled with multi-path reflection interference. The experimental setup is depicted in Fig. 10. The base-band signal is generated by the NI USRP-2954, with a symbol rate of 125 kHz and 16-QAM modulation. The center carrier frequency of the Intermediate Frequency (IF) signal is 2.8 GHz. After frequency up-conversion by the mixer to 10.7 GHz, it is radiated into free space by a horn antenna. The transmitting antenna is positioned 2.5 meters away from the RIS. After modulation by the RIS, the transmitted signal is directionally reflected to different near-field spatial regions. Another horn antenna serves as the mobile receiving user, which will capture the RF signals reflected by the RIS. After down-conversion, another USRP-2954 is responsible for demodulation to recover the baseband data from the transmitter. The data is transmitted using single-carrier transmission without channel coding. For clarity, the main experimental parameters have been listed in Table 2.

As illustrated in Fig. 10, the LabVIEW interface connected to USRPs allows the real-time observation of the demodulation constellation and Rx eye diagram. At the transmitter, a set of random sequences is cyclically transmitted as the original communication data in this experiment. The receiving user stores sufficiently long sequence data and systematically compares it with the original transmitted sequence to statistically evaluate the demodulation Bit Error Rate (BER) performance. During the experiment,

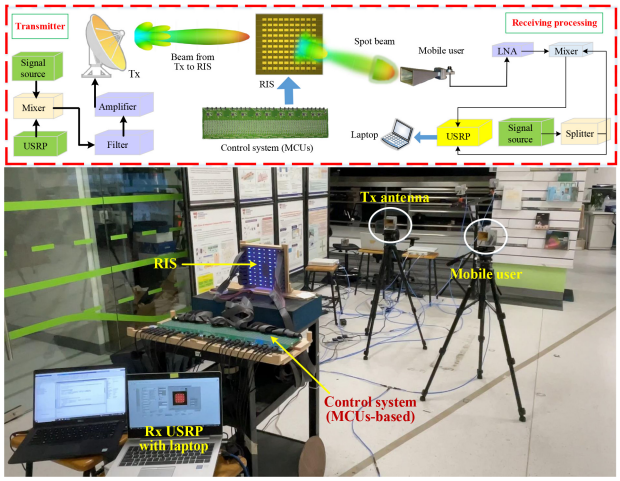

FIGURE 10. The basic setup and on-site view of the experiment.

TABLE 2. Main experiment parameters.

Parameter	Value	Dimension
Central carrier frequency	10.7	GHz
Intermediate frequency	2.8	GHz
Samples per symbol	8	-
Baseband bandwidth	125	kHz
Tx antenna gain	15	dB
Transmitting power	0	dBm
Rx antenna gain	15	dB
Low Noise Amplifier (LNA)	20	dB
Modulation for pilot signal	16-QAM	-
Modulation for data stream	16-QAM	-

the spatial position of the horn antenna is changed to simulate the random movement of the mobile user. During the movement, the RIS together with its control system dynamically changes the codebook state in real time based on the pre-defined algorithm illustrated in Section III. Then, the shape of the reflected beams will be altered, enabling the tracking of the user's movement and achieving real-time stable data transmission (Recorded video is at https://youtu.be/riBH0YZBXtk).

It should be noted that some tracking delays were observed during the experiment, primarily attributable to the lower completion level of our prototyping. In this setup, significant time was consumed by data collection and command execution processes within LabView and MATLAB. However, in the commercial product phase, the time required for the RIS to reconfigure itself would be considerably reduced, as all algorithms would already be embedded into the MCU chips. Furthermore, when the RIS is implemented in a real mobile network, it will include data packet redundancy and retransmission protocols. These mechanisms will ensure the complete reception of useful information, even in the event of brief link interruptions, thereby maintaining the actual communication experience of the mobile users.

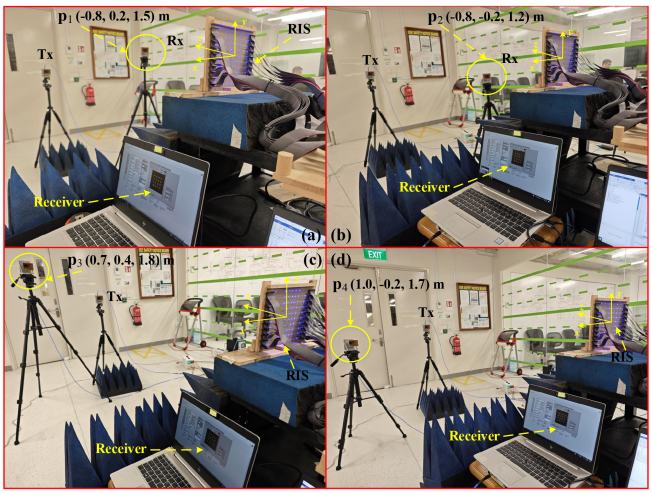

FIGURE 11. Measurement scenarios at different 3D spatial receiving regions with respect to (a) location p_1 (b) location p_2 (c) location p_3, and (d) location p_4. (Tx antenna gain 15 dB, Tx power 0 dBm, Rx antenna gain 15 dB, Rx LNA 20 dB, bandwidth 125 kHz).

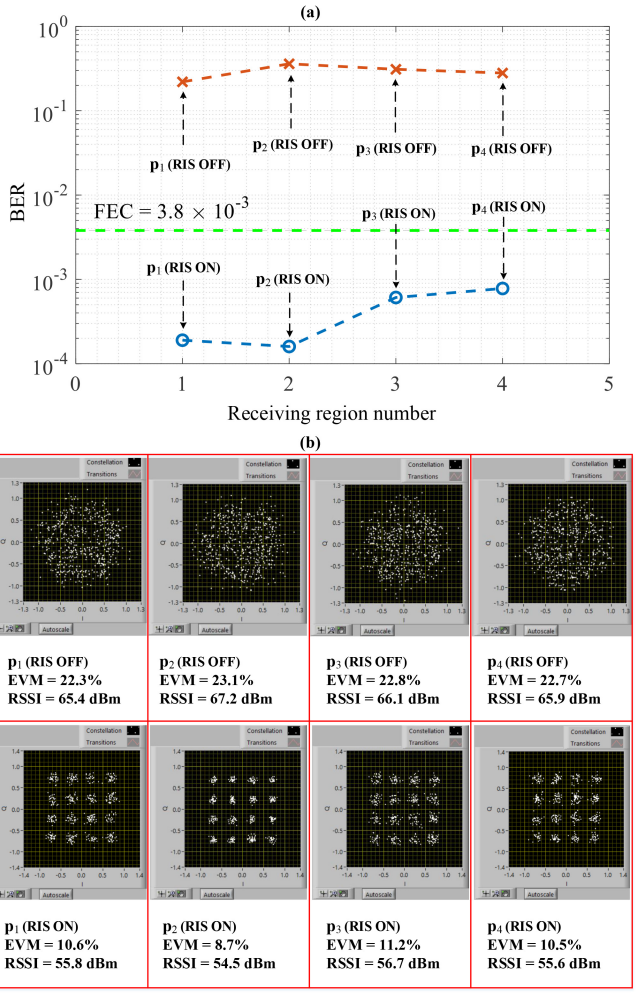

FIGURE 12. The constellation diagrams and BER measurement results at different 3D spatial receiving regions when the RIS is OFF and ON (optimized). (a) BER comparing results at different spatial locations. (b) Constellation diagrams, EVM, and RSSI measurement results.

Without loss of generality, considering the RIS center as the origin, we selected four spatial coordinates at varying distances and heights from the RIS to verify the 3D spot beamforming efficiency, namely, $\mathbf{p}_1 = (-0.8, 0.2, 1.5)$m, $\mathbf{p}_2 = (-0.8, -0.2, 1.2)$m, $\mathbf{p}_3 = (0.7, 0.4, 1.8)$m, $\mathbf{p}_4 = (1.0, -0.2, 1.7)$m. Subsequently, the RX antenna is sequentially moved to the corresponding coordinates, as shown in Fig. 11. In the experiments, we measure and compare the Received Signal Strength Indicator (RSSI) under both RIS ON (optimized) and OFF states. The actual measurement results from different 3D spatial regions are recorded in Fig. 12. It is obvious that when the RIS is in the OFF state or ON (optimized) state, the RSSI in the corresponding reception region differs by more than 10 dB. Then, at each of the four distinct spatial regions, the user antenna holds for a few seconds, ensuring that the receiving USRP collects and records a sufficient length of the receiving data for BER calculation. The statistical results are also depicted in Fig. 12. Obviously, when RIS is ON (optimized) with the specific spot beam pattern, the BER statistical results at all reception regions are far below the Forward Error Correction (FEC) limit (3.8×10^{-3}) [36], indicating that the RIS can automatically adjust the optimal codebook with the movement of the user, achieving beam tracking and ensuring the stability of communications. When the RIS is in the OFF state, the receiver cannot capture sufficient signal energy, resulting in a severe deterioration of the constellation diagram and BER metrics.

IV. ROTATIONAL VORTEX WAVEFRONT MANIPULATION THROUGH SPACE-TIME DIGITAL CODING ON RIS PROTOTYPING

Moreover, to substantiate the rapid-response programmable and full-array independent control capacities of the RIS prototyping developed in this study, we utilize a phase-shifting scheme for producing time-varying rotational vortex beams. This approach leverages the unique properties of vortex beams, which possess angular momentum owing to their helical wavefronts, to subtly and swiftly modulate the phase distribution throughout the RIS board.

Vortex beams, also known as Orbital Angular Momentum (OAM) beams, are characterized by a helical phase front. The phase of the beam twists around the beam axis, resulting in a spiral wavefront. These beams carry OAM, which can be utilized for various advanced communication techniques [37]. The fast rotation of the wavefront in vortex beams creates a dynamic phase variation over time. When the RIS is used to generate and manipulate these vortex beams, it can induce rapid changes in the phase distribution of the reflected waves. This rapid phase variation is analogous to the Doppler shift, in other words, the rotational wavefront of the OAM beam causes the carrier phase to change more rapidly over time, resulting in a shift of the carrier's

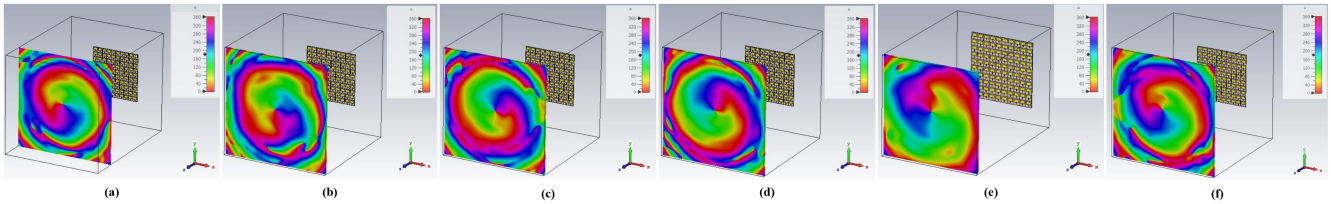

FIGURE 13. Spinning vortex beams to generate rotational Doppler shift based highly dynamic RIS and phase-shifting scheme. (a) $l = 1$, $t = 0$. (b) $l = 1$, $t = T/6$. (c) $l = 1$, $t = 2T/6$. (d) $l = 1$, $t = 3T/6$. (e) $l = 1$, $t = 4T/6$. (f) $l = 1$, $t = 5T/6$.

central frequency in the frequency domain. This has been verified by a lot of previous studies [38], [39], [40], [41]. Therefore, in the Doppler domain, by rotating the vortex beam's wavefront, we can effectively modulate the signal frequency. The rotation speed of the wavefront and the OAM topological mode determine the rate of this modulation, creating a Doppler-like effect even in the absence of actual motion. This technique can be employed to modulate signals for various applications, such as enhancing communication robustness or encoding additional information in the phase of the signal.

A. ROTATIONAL VORTEX BEAMS GENERATION BY RIS

As we know, by introducing an azimuthal phase factor, $\exp(*)$, into an EM beam, it is possible to generate an OAM EM wave with a helical phase front. Traditional time-invariant azimuthal phase factors can be represented as $\exp(jl\phi)$, where l denotes the topological mode of the vortex beam, and ϕ is the azimuthal angle. Then, the vortex beam can be expressed as,

$$E(\phi, t) = A_e \exp(j2\pi f_0 t) \exp(j\delta(\phi)), \tag{9}$$

where A_e is the amplitude constant related to the antenna system, f_0 is the center carrier frequency. Hence, the entire metasurface can be divided into 4 distinct regions along the azimuths direction, corresponding to 4 continuously varying phase states, thereby generating vortex beams, as shown in Fig. 14.

By further introducing time-varying characteristics and sequentially altering the initial phase of the azimuthal phase factor across different time slots, we can achieve a spatiotemporally modulated phase, which has been illustrated in Fig. 13. This modulated phase, which incorporates both spatial and temporal variations, can be expressed as,

$$\delta(\phi, t) = jl\phi + 2\pi l \cdot t/T + \Delta, \tag{10}$$

where T denotes the period of rotation, t is the time variable, Δ is the random initial phase. Furthermore, by differentiating (10) with respect to time, we can derive the expression for the Doppler frequency shift induced by the rotation of an EM beam carrying a vortex wavefront. Specifically, this can be represented as,

$$\Delta f = \frac{1}{2\pi} \frac{d\delta(\phi, t)}{dt} = \frac{l}{T}. \tag{11}$$

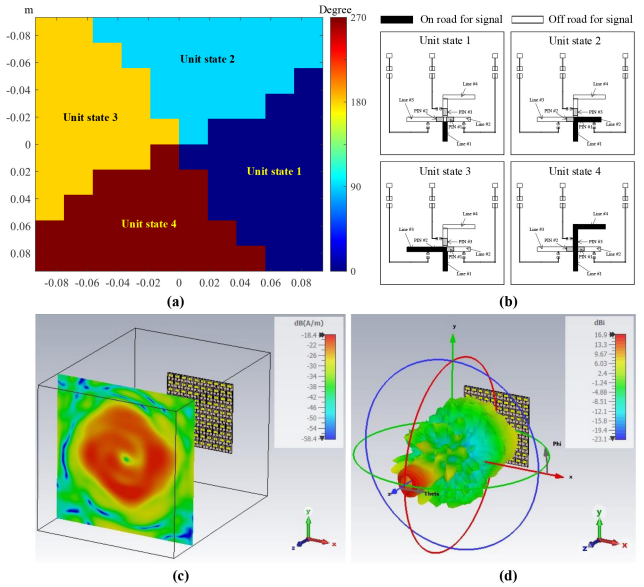

FIGURE 14. Vortex beam generation with RIS. (a) Phase distribution on the RIS. (b) Unit states illustrations. (c) Energy distribution in a cross-section perpendicular to the beam propagation direction. (d) Radiation pattern of vortex mode 1.

It is evident that the magnitude of the Doppler frequency shift is jointly determined by the temporal modulation period T of the RIS and the vortex topological mode number l.

B. ARTIFICIAL DOPPLER SHIFT MEASUREMENT WITH HIGHLY DYNAMIC TIME-VARYING ROTATIONAL VORTEX BEAMS

Through precise alterations of the time-varying vortex beams generated by the RIS, we achieve dynamic control over artificial Doppler shifts within the signal frequency domain. This capability not only demonstrates the RIS prototyping's highly dynamic beamforming potential but also highlights its utility in enhancing various application scenarios through sophisticated manipulation of EM waves, e.g., Doppler radar velocity deception and stealth [40], [41]. A specific example has been illustrated in Fig. 13, which describes how we rotated the vortex beams in detail, and the artificial Doppler experiment setup and measurement results are shown in Fig. 15 (Recorded video is at https://youtu.be/IJDO-I-umaI).

In our experiments, we utilized a spectrum analyzer (Agilent E4440A) to measure the center frequency of the single-carrier signal reflected by the RIS in a stationary state, as well as the frequency spectrum of the signal when the

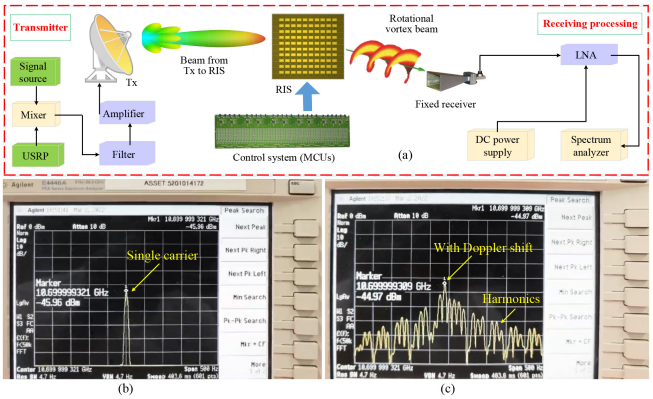

FIGURE 15. Measured spectrum with rotational Doppler generated by the RIS prototyping. (a) Vortex beam experiment setup. (b) Single carrier without Doppler shift. (c) Single carrier with rotational Doppler shift. (Tx antenna gain 15 dB, Tx power 10 dBm, Rx antenna gain 15 dB, Rx LNA 20 dB, single carrier).

RIS was in space-time digital-coding states. The comparative results of their spectra are illustrated in Fig. 15(a)(b). It is distinctly observable that when the RIS generates a vortex undergoing rapid wavefront rotation through space-time digital-coding, the center frequency of the carrier signal shifts by $\Delta f = 12$ Hz. In the experiment, we employed rapid switching among 12 different vortex wavefront states ($l = 1$) continuously, implying that the time required for the RIS to switch between each vortex state is approximately $\frac{1}{12\times\Delta f}$ seconds. This observation aligns with the calculations presented in Section II-B, further corroborating the rapid-response control capabilities of our RIS prototyping for EM beam manipulation. Moreover, this experiment demonstrates that by adjusting the temporal modulation parameters and selecting specific vortex modes, it is possible to finely tune the Doppler shift. This experimental evidence highlights the prototyping's advanced functionality in precisely manipulating electromagnetic waves, demonstrating its potential for high-speed, dynamic wireless communication applications. This research blurs the boundary between RF antennas and digital signal processing, offering a new perspective for studying encoded EM environment signal processing. Some new digital signal processing algorithms can be designed based on this finding, e.g., OTFS technology applied in low mobility scenarios based on artificial Doppler shift generated by the RIS-OAM system [42].

V. OUTDOOR FAR-FIELD BEAMFORMING TESTING UNDER BLOCKING SCENARIOS

Furthermore, for outdoor far-field application scenarios, our RIS prototyping also demonstrates its ability to efficiently distribute energy to specified areas through the manipulation of beam directions. This capability is particularly important for non-line-of-sight users obstructed by buildings. To validate the capability of the RIS board with this 10×10 size to modulate radio waves in natural environments, we conducted a comparative validation experiment on an outdoor balcony and corridor near our lab, as shown in Fig. 16. This approach

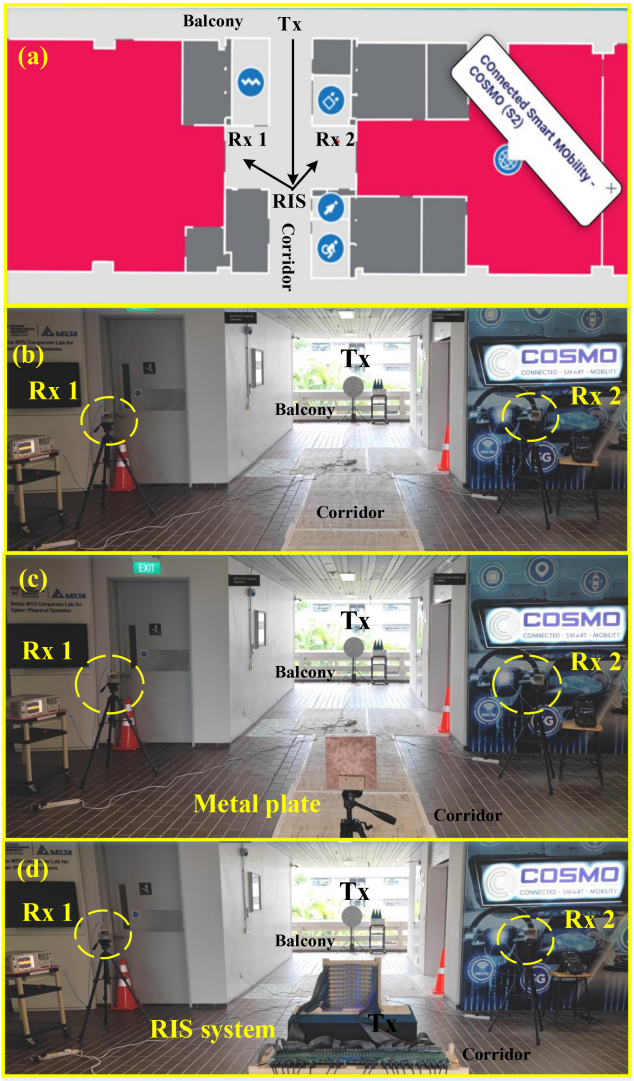

FIGURE 16. RIS comparative experiments in the outdoor far-field scenario. (a) Diagram of the experimental setup. (b) In the line-of-sight corridor, without reflective objects. (c) In the line-of-sight corridor, featuring a metal plate of the same size as the RIS to enhance signal reflection. (d) In the line-of-sight corridor, utilizing the RIS to modulate signal reflection. (Tx reflector antenna gain 30 dB, Tx power 20 dBm, Rx antenna gain 15 dB, Rx LNA 20 dB, single carrier).

ensures that the RIS's effectiveness in manipulating EM waves is tested under conditions that closely mimic real-world scenarios, thus providing a robust assessment of its practical application potential in outdoor wireless scenarios. To mitigate interference with other commercial frequency bands, all the outdoor experiments are operated in the X-band. The transmission setup features a reflector antenna that emits a single-carrier signal directly from the RF signal source with an extremely narrow beam illuminating the RIS board. This signal follows a line-of-sight path to the RIS, which then reflects it toward receivers located in the corners of the corridor. At the receiving end, a standard-gain directional horn antenna captures the signal. Notably, due to obstructions like wall corners and the directional

TABLE 3. Receiving power captured by the microwave analyzer (Keysight, N9917A) in testing scenarios shown by Fig. 16.

Scenarios	Rx 1	Rx 2
No reflective objects	-61.8 dBm	-60.7 dBm
Rx 1 at about 0° to metal plate	-45.1 dBm	NA
Rx 1 move 15° to metal plate	-54.7 dBm	NA
RIS beam sweep to Rx 1 $(+45^\circ, 4m)$	-46.6 dBm	-55.2 dBm
RIS beam sweep to Rx 2 $(-30^\circ, 4m)$	-54.3 dBm	-45.8 dBm

characteristics of the antennas, there is no direct line-of-sight connection between the transmitter and receiver.

To provide a comparative analysis with the RIS-aided communication link, we set up two additional scenarios as control groups, as depicted in Fig. 16(b) and 16(c). In scenario Fig. 16(b), no reflective objects are placed directly in front of the transmitter. The signal is emitted by the Tx antenna from a balcony on one side of the building, traverses the corridor, and radiates into free space from a balcony on the opposite side. In contrast, scenario Fig. 16(c) features a metal plate of similar dimensions positioned at the same location as the RIS along the direct signal propagation path. Upon reflecting off the metal plate, the energy of the signal is captured by the receiving antenna at both mirrored and non-mirrored reflection directions, which is then compared to the scenario with an RIS present, as shown in Fig. 16(d). At the receiver's location, a spectrum analyzer is employed to record and compare the variations in reflected signal energy. The experimental results are tabulated in Table 3.

From experimental results, it's evident that in the absence of any reflective objects along the direct line-of-sight path, the receiver can only receive the signal power of around -60 dBm by random reflections. When a metal plate is introduced into this direct path, a noticeable increase in received power to approximately -45.1 dBm is observed along the normal direction of the metal plate. However, as one deviates from this normal direction, the received signal power rapidly diminishes. This suggests that the metal plate can only provide specular reflection and is not adaptable to mobile communication environments. Subsequently, we replaced the metal plate with an RIS panel of equivalent dimensions and positioned the receiver at angles of -30°, 4 m and 45°, 4 m relative to the RIS. By employing MCUs-controlled RIS to steer reflected beams to various locations, significant variations in received power were observed, as detailed in Table 3.

For instance, when the RIS adjusts the direction of the reflected beam towards $+45^\circ$, the received power at Rx 1 is approximately -46.6 dBm. Conversely, when the beam is steered towards a non-mirror-symmetric angle, i.e., -30° direction, the received power at Rx 1 direction drops by about 10 dB, while the received power at Rx 2 direction elevates to -45.8 dBm. Similarly, when the RIS-controlled beam is redirected from Rx 2 towards Rx 1, which is not mirror-symmetric, the received power at Rx 1 increases, while the received power at Rx 2 decreases to -55.2 dBm. It is evident that higher receiving power leads to an improved signal-to-noise ratio, thereby enhancing the demodulation performance at the receiver. This not only demonstrates that our RIS prototyping offers flexible beamforming capabilities, but also proves that even under outdoor far-field conditions, an RIS board of this size can still provide a considerable increase in received power for obstructed users. This has significant implications for deep coverage and ensuring communication quality in mobile communication scenarios.

It is worth emphasizing that while a simple metal reflector can provide basic signal reflection, RIS technology offers significant advantages that justify its practicality and necessity. RIS provides dynamic beamforming and steering, allowing it to adjust the phase and amplitude of reflected signals in real-time, optimize signal strength, and coverage dynamically. Additionally, RIS actively mitigates interference, improves energy efficiency through targeted reflection, and supports advanced functionalities like secure communication, environmental sensing, and spatial modulation. Our experiments in Fig. 16 and Table 3 demonstrate that even a small RIS prototype can enhance signals effectively in practical scenarios, proving its superiority in dynamic and varied real-world applications.

VI. CONCLUSION AND DISCUSSION

This paper has unveiled an exhaustive exploration into the design, implementation, and experimental validation of an innovative 2-bit reconfigurable metasurface prototyping, characterized by its capability for full-array flexible control and rapid-response to control inputs. This prototyping facilitates a plethora of wireless solutions, including 3D spot beam tracing, artificial rotational Doppler modulation by time-varying vortex beams, and outdoor far-field beam steering. Notably, the prototyping achieves rapid switching of the entire RIS array's patterns of less than 1 millisecond, which may enable it to track fast-moving targets such as small UAVs, bicycles, and cars navigating urban roads in the future, and offer a new perspective for studying encoded EM environment signal processing.

Central to our investigation is the introduction of a novel 2-bit phase-quantized unit cell design which is distinguished by its capability to maintain 4 stable phase states with 90° differences, an energy attenuation of less than 0.6 dB across a bandwidth of 200 MHz, and full-array flexible independent control. By achieving such low insertion loss while providing multiple phase configurations, our prototyping offers a robust platform for the development of advanced wireless solutions. Supported by a programmable hardware architecture and enhanced by the parallel processing and pre-configuration capabilities of meticulously designed multi-MCU control circuits, this system embodies the epitome of rapid and precise phase adjustment capabilities. This foundation enables the execution of complex structured EM waves, allowing for the dynamic manipulation of the EM wavefront to meet the demanding requirements of modern wireless technologies.

Moreover, this study develops a tailored spot beamforming codebook scheme for RIS-aided 3D spot beam tracking. Introducing an adaptable and efficient RIS scanning algorithm, this system facilitates the dynamic and robust communication link for moving users.

Reflecting on this research, we recognize that the contributions of this paper extend the horizons of reconfigurable metasurface technologies, offering fresh perspectives for future explorations, e.g., integration of RIS with existing wireless standards, high-efficient wireless power transfer, integrated sensing and communication, etc. The promise held within the pages of this paper is but a glimpse into the future, where the confluence of RIS and wireless technologies transforms the landscape of how we connect, power, and perceive the world around us.

REFERENCES

[1] C. Huang et al., "Holographic MIMO surfaces for 6G wireless networks: Opportunities, challenges, and trends," *IEEE Wireless Commun.*, vol. 27, no. 5, pp. 118–125, Oct. 2020, doi: 10.1109/MWC.001.1900534.

[2] P. Mursia, F. Devoti, V. Sciancalepore, and X. C.-Pérez, "RISe of Flight: RIS-empowered UAV communications for robust and reliable air-to-ground networks," *IEEE Open J. Commun. Soc.*, vol. 2, pp. 1616–1629, 2021, doi: 10.1109/OJCOMS.2021.3092604.

[3] J. Wang et al., "Interplay between RIS and AI in wireless communications: Fundamentals, architectures, applications, and open research problems," *IEEE J. Sel. Areas Commun.*, vol. 39, no. 8, pp. 2271–2288, Aug. 2021, doi: 10.1109/JSAC.2021.3087259.

[4] S. Kisseleff, W. A. Martins, H. Al-Hraishawi, S. Chatzinotas, and B. Ottersten, "Reconfigurable intelligent surfaces for smart cities: Research challenges and opportunities," *IEEE Open J. Commun. Soc.*, vol. 1, pp. 1781–1797, 2020, doi: 10.1109/OJCOMS.2020.3036839.

[5] Z. X. Wang, H. Q. Yang, F. Zhai, J. W. Wu, Q. Cheng, and T. J. Cui, "A low-cost and low-profile electronically programmable bit array antenna for two-dimensional wide-angle beam steering," *IEEE Trans. Antennas Propag.*, vol. 71, no. 1, pp. 342–352, Jan. 2023, doi: 10.1109/TAP.2022.3221840.

[6] L. Zhu et al., "Dual linearly polarized 2-bit programmable metasurface with high cross-polarization discrimination," *IEEE Trans. Antennas Propag.*, vol. 72, no. 2, pp. 1510–1520, Feb. 2024, doi: 10.1109/TAP.2023.3345034.

[7] J. Zhu, K. Liu, Z. Wan, L. Dai, T. J. Cui, and H. V. Poor, "Sensing RISs: Enabling dimension-independent CSI acquisition for beamforming," *IEEE Trans. Inf. Theory*, vol. 69, no. 6, pp. 3795–3813, Jun. 2023, doi: 10.1109/TIT.2023.3243836.

[8] S. Yue, S. Zeng, H. Zhang, F. Lin, L. Liu, and B. Di, "Intelligent omni-surfaces aided wireless communications: Does the reciprocity hold?" *IEEE Trans. Veh. Technol.*, vol. 72, no. 6, pp. 8181–8185, Jun. 2023, doi: 10.1109/TVT.2023.3242283.

[9] H. Zhang, X. Chen, Z. Wang, Y. Ge, and J. Pu, "A 1-bit electronically reconfigurable reflectarray antenna in X band," *IEEE Access*, vol. 7, pp. 66567–66575, 2019, doi: 10.1109/ACCESS.2019.2918231.

[10] M. Wang, S. Xu, F. Yang, and M. Li, "A 1-bit bidirectional reconfigurable transmit-reflect-array using a single-layer slot element with PIN diodes," *IEEE Trans. Antennas Propag.*, vol. 67, no. 9, pp. 6205–6210, Sep. 2019, doi: 10.1109/TAP.2019.2925925.

[11] H. Luyen, J. H. Booske, and N. Behdad, "2-bit phase quantization using mixed polarization-rotation/non-polarization-rotation reflection modes for beam-steerable reflectarrays," *IEEE Trans. Antennas Propag.*, vol. 68, no. 12, pp. 7937–7946, Dec. 2020, doi: 10.1109/TAP.2020.3000517.

[12] X. Hu, R. Deng, B. Di, H. Zhang, and L. Song, "Holographic beamforming for ultra massive MIMO with limited radiation amplitudes: How many quantized bits do we need?" *IEEE Commun. Lett.*, vol. 26, no. 6, pp. 1403–1407, Jun. 2022, doi: 10.1109/LCOMM.2022.3151801.

[13] L. Zhang et al., "Breaking reciprocity with space-time-coding digital metasurfaces," *Adv. Mater.*, vol. 31, no. 41, Oct. 2019, Art. no. 1904069, doi: 10.1002/adma.201904069.

[14] H. Kamoda, T. Iwasaki, J. Tsumochi, T. Kuki, and O. Hashimoto, "60-GHz electronically reconfigurable large reflectarray using single-bit phase shifters," *IEEE Trans. Antennas Propag.*, vol. 59, no. 7, pp. 2524–2531, Jul. 2011, doi: 10.1109/TAP.2011.2152338.

[15] L. Wang et al., "A review of THz modulators with dynamic tunable metasurfaces," *Nanomaterials*, vol. 9, no. 7, p. 965, Jul. 2019, doi: 10.3390/nano9070965.

[16] J. Liao, S. Guo, L. Yuan, C. Ji, C. Huang, and X. Luo, "Independent manipulation of reflection amplitude and phase by a single-layer reconfigurable metasurface," *Adv. Opt. Mater.*, vol. 10, no. 4, Dec. 2021, Art. no. 2101551, doi: 10.1002/adom.202101551.

[17] Q. Cheng et al., "Reconfigurable intelligent surfaces: Simplified-architecture transmitters—From theory to implementations," *Proc. IEEE*, vol. 110, no. 9, pp. 1266–1289, Sep. 2022, doi: 10.1109/JPROC.2022.3170498.

[18] C. Liu, F. Yang, S. Xu, and M. Li, "Reconfigurable metasurface: A systematic categorization and recent advances," Jan. 2023, *arXiv:2301.00593*.

[19] C.-C. Cheng and A. A.-Tamijani, "Study of 2-bit antenna-filter-antenna elements for reconfigurable millimeter-wave lens arrays," *IEEE Trans. Microw. Theory Techn.*, vol. 54, no. 12, pp. 4498–4506, Dec. 2006, doi: 10.1109/TMTT.2006.885993.

[20] Y. Yin et al., "Design of a 2-bit dual-polarized reconfigurable reflectarray with high aperture efficiency," *IEEE Trans. Antennas Propag.*, vol. 72, no. 1, pp. 542–552, Jan. 2024, doi: 10.1109/TAP.2023.3326951.

[21] L. G. da Silva, P. Xiao, and S. A. Cerqueira, "A 2-bit tunable unit cell for 6G reconfigurable intelligent surface application," in *Proc. 16th Eur. Conf. Antennas Propag. (EuCAP)*, Madrid, Spain, 2022, pp. 1–5, doi: 10.23919/EuCAP53622.2022.9769482.

[22] S. Zeng et al., "RIS-based IMT-2030 testbed for mmWave multi-stream ultra-massive MIMO communications," *IEEE Wireless Commun.*, vol. 31, no. 3, pp. 375–382, Jun. 2024, doi: 10.1109/MWC.005.2300052.

[23] L. Dai et al., "Reconfigurable intelligent surface-based wireless communications: Antenna design, prototyping, and experimental results," *IEEE Access*, vol. 8, pp. 45913–45923, 2020, doi: 10.1109/ACCESS.2020.2977772.

[24] M. Rossanese, P. Mursia, A. Garcia-Saavedra, V. Sciancalepore, A. Asadi, and X. C.-Perez, "Designing, building, and characterizing RF switch-based reconfigurable intelligent surfaces," in *Proc. 16th ACM Workshop Wireless Netw. Testbeds, Exp. Eval. Characterization (WiNTECH)*, 2022, pp. 69–76, doi: 10.1145/3556564.3558236.

[25] J.-B. Gros, V. Popov, M. A. Odit, V. Lenets, and G. Lerosey, "A reconfigurable intelligent surface at mmWave based on a binary phase tunable metasurface," *IEEE Open J. Commun. Soc.*, vol. 2, pp. 1055–1064, 2021, doi: 10.1109/OJCOMS.2021.3076271.

[26] R. Wang, Y. Yang, B. Makki, and A. Shamim, "A wideband reconfigurable intelligent surface for 5G millimeter-wave applications," *IEEE Trans. Antennas Propag.*, vol. 72, no. 3, pp. 2399–2410, Mar. 2024, doi: 10.1109/TAP.2024.3352828.

[27] J. Zhao, et al., "Programmable time-domain digital-coding metasurface for non-linear harmonic manipulation and new wireless communication systems," *Nat. Sci. Rev.*, vol. 6, no. 2, pp. 231–238, Mar. 2019, doi: 10.1093/nsr/nwy135.

[28] J. Y. Dai, J. Zhao, Q. Cheng, and T. J. Cui, "Independent control of harmonic amplitudes and phases via a time-domain digital coding metasurface," *Light Sci. Appl.*, vol. 7, no. 1, p. 90, 2018, doi: 10.1038/s41377-018-0092-z.

[29] L. Zhang and T. J. Cui, "Angle-insensitive 2-bit programmable coding metasurface with wide incident angles," in *Proc. IEEE Asia–Pacific Microw. Conf. (APMC)*, Singapore, 2019, pp. 932–934, doi: 10.1109/APMC46564.2019.9038764.

[30] M. Cui, Z. Wu, Y. Lu, X. Wei, and L. Dai, "Near-field MIMO communications for 6G: Fundamentals, challenges, potentials, and future directions," *IEEE Commun. Mag.*, vol. 61, no. 1, pp. 40–46, Jan. 2023, doi: 10.1109/MCOM.004.2200136.

[31] Y. Liu, Z. Wang, J. Xu, C. Ouyang, X. Mu, and R. Schober, "Near-field communications: A tutorial review," *IEEE Open J. Commun. Soc.*, vol. 4, pp. 1999–2049, 2023, doi: 10.1109/OJCOMS.2023.3305583.

[32] H. Lu and Y. Zeng, "Communicating with extremely large-scale array/surface: Unified modeling and performance analysis," *IEEE Trans. Wireless Commun.*, vol. 21, no. 6, pp. 4039–4053, Jun. 2022, doi: 10.1109/TWC.2021.3126384.
[33] Sadeghian, M., Pizzo, A., and Lozano, A. "RIS in indoor environments: Benchmarking against ambient propagation," 2023, *arXiv:2311.05266*.
[34] Y. Zhao et al., "Holographic-inspired meta-surfaces exploiting vortex beams for low-interference multipair IoT communications: From theory to prototype," *IEEE Internet Things J.*, vol. 11, no. 7, pp. 12660–12675, Apr. 2024, doi: 10.1109/JIOT.2023.3334746.
[35] I. M. Salom, A. V. Kabovic, M. M. Kabovic, J. J. Gajica, and V. V. Ćelebić, "Implementation of NTP protocol in an isolated corporate network," in *Proc. 27th Telecommun. Forum (TELFOR)*, Belgrade, Serbia, 2019, pp. 1–4, doi: 10.1109/TELFOR48224.2019.8971119.
[36] J. R. Barry, E. A. Lee, and D. G. Messerschmitt, *Digital communication*, 3rd. Cham, Switzerland: Springer, 2004.
[37] Y. Zhao, Z. Wang, Y. Lu, and Y. L. Guan, "Multimode OAM convergent transmission with co-divergent angle tailored by airy wavefront," *IEEE Trans. Antennas Propag.*, vol. 71, no. 6, pp. 5256–5265, Jun. 2023, doi: 10.1109/TAP.2023.3263920.
[38] C. Zhang, L. Ma, "Millimetre wave with rotational orbital angular momentum," *Sci. Rep.*, vol. 6, Sep. 2016, Art. no. 31921, doi: 10.1038/srep31921.
[39] C. Zhang and L. Ma, "Detecting the orbital angular momentum of electro-magnetic waves using virtual rotational antenna," *Sci. Rep.*, vol. 7, p. 4585, Jul. 2017, doi: 10.1038/s41598-017-04313-4.
[40] J. Zhang, P. Li, R. C. C. Cheung, A. M. H. Wong, and J. Li, "Generation of time-varying orbital angular momentum beams with space-time-coding digital metasurface," *Adv. Photon.*, vol. 5, no. 3, Apr. 2023, Art. no. 36001, doi: 10.1117/1.AP.5.3.036001.
[41] B. Liu, H. Chu, H. Giddens, R. Li, and Y. Hao, "Experimental observation of linear and rotational doppler shifts from several designer surfaces," *Sci. Rep.*, vol. 9, p. 8971, Jun. 2019, doi: 10.1038/s41598-019-45516-1.
[42] Y. Zhao et al., "OAM-based reconfigurable doppler shifts enable PAPR reduction for multi-carrier doppler diversity," in *Proc. Asia–Pacific Microw. Conf. (APMC)*, Yokohama, Japan, 2022, pp. 485–487, doi: 10.23919/APMC55665.2022.9999832.

YUFEI ZHAO received the B.Eng. degree (Outstanding Graduates) in electronic information engineering from the Harbin Institute of Technology, China, in 2014, and the Ph.D. degree in aeronautical and astronautical science and technology from Tsinghua University, China, in 2020.

From 2020 to 2021, he worked as a Senior Engineer with Huawei Technologies Company Ltd., China. He is currently a Research Fellow with the School of Electrical and Electronic Engineering, Nanyang Technological University, Singapore. His current research interests include wireless communication engineering, RF & microwave system, reconfigurable intelligent surface, and electromagnetic wave transmission with orbital angular momentum.

Dr. Zhao was also the recipient of the Young Scientist Award in Singapore Workshop on Antenna in 2022. He serves as a Reviewer for IEEE TRANSACTIONS ON ANTENNAS AND PROPAGATION, IEEE TRANSACTIONS ON WIRELESS COMMUNICATIONS, IEEE TRANSACTIONS ON VEHICULAR TECHNOLOGY, and IEEE INTERNET OF THINGS JOURNAL.

YUAN FENG received the B.S. degree from Southeast University, Nanjing, China, in 2014, and the Ph.D. degree from Tsinghua University, Beijing, China, in 2020.

He is currently a Research Fellow with the National University of Singapore, Singapore. His research interests include wireless communication technology, reconfigurable antenna implantable antenna, and the application of electromagnetics and antenna technology in biomedical science and engineering.

Dr. Feng is a Reviewer of IEEE TRANSACTIONS ON ANTENNAS AND PROPAGATION, IEEE TRANSACTIONS ON BIOMEDICAL CIRCUITS AND SYSTEMS, *Frontiers in Physics*, and *Engineering*.

AFKAR MOHAMED ISMAIL received the B.Eng. degree in electrical and electronics engineering from the South Eastern University of Sri Lanka, Sri Lanka in 2021, where he worked as an Instructor with the Department of Computer Science and Engineering. He is currently a Research Engineer with the School of Electrical and Electronic Engineering, Nanyang Technological University, Singapore. He possesses skills in PCB design, firmware development, and MCU programming.

ZIYUE WANG received the B.Eng. degree in electronic and information from Beijing Jiaotong University in 2023. He is currently pursuing the master's degree with the School of Electrical and Electronic Engineering, Nanyang Technological University, Singapore. He possesses skills in software defined radio design. His research interests include RIS and wireless signal processing.

YONG LIANG GUAN (Senior Member, IEEE) received the Bachelor of Engineering degree (With First Class Hons.) from the National University of Singapore, and the Ph.D. degree from Imperial College London, U.K.

He is currently a Professor of Communication Engineering with the School of Electrical and Electronic Engineering, Nanyang Technological University (NTU), Singapore, where he leads the Continental-NTU Corporate Research Lab and led the successful deployment of the campus-wide NTU-NXP V2X Test Bed. He is also currently an Associate Vice President of NTU. He has published an invited monograph, two books, and more than 450 journal and conference papers. He has secured over S$70 million of external research funding. He has 15 filed patents and three granted patents, one of which was licensed to NXP Semiconductors. His research interests broadly include coding and signal processing for communication systems and data storage systems.

Dr. Guan is an Editor of the IEEE TRANSACTIONS ON VEHICULAR TECHNOLOGY. He is a Distinguished Lecturer of the IEEE Vehicular Technology Society.

YONGXIN GUO (Fellow, IEEE) received the B.Eng. and M.Eng. degrees in electronic engineering from the Nanjing University of Science and Technology, Nanjing, China, in 1992 and 1995, respectively, and the Ph.D. degree in electronic engineering from the City University of Hong Kong, Hong Kong, in 2001.

He is currently a Chair Professor of Electronic Engineering under the Global STEM Professorship Scheme with the Department of Electrical Engineering, City University of Hong Kong. He was a Professor with the Department of Electrical and Computer Engineering, National University of Singapore (NUS). He has authored or co-authored over 600 international journal and conference papers, two books and four book chapters. He holds over 70 granted/filed patents in USA, China, and Singapore. He has graduated 24 Ph.D. students and hosted and supervised more than 110 research staff, visiting Ph.D. students, and visiting scholars with NUS. His current research interests include electromagnetics in biomedicine, antennas, microwave, millimeter-wave and terahertz integrated circuits, wireless power transfer, radar systems, microwaves in quantum computing, AI for antennas, RF circuits, and wireless sensing.

Dr. Guo received the CityU HK 1st EE Outstanding Alumni Award in 2022. He was the recipient of 2020 IEEE Microwave and Wireless Components Letters Tatsuo Itoh Prize of the IEEE Microwave Theory and Techniques Society. He is serving as the IEEE Biomedical Engineering Award Committee and served as the IEEE Fellow Evaluation Committee for IEEE Engineering in Medicine and Biology Society from 2019 to 2020. He served as an Associate Editor for IEEE ANTENNAS AND PROPAGATION MAGAZINE from 2018 to 2020, IEEE JOURNAL OF ELECTROMAGNETICS, RF AND MICROWAVE IN MEDICINE AND BIOLOGY from 2017 to 2020, *Electronics Letters* from 2015 to 2019, IEEE ANTENNAS AND WIRELESS PROPAGATION LETTERS from 2013 to 2018, and *IET Microwaves, Antennas and Propagation* from 2014 to 2017. He is serving as the Editor-in-Chief for IEEE JOURNAL OF ELECTROMAGNETICS, RF AND MICROWAVE IN MEDICINE AND BIOLOGY from 2020 to 2025. He has served as the General Chair/Co-Chair for a number of international conferences/workshops. He was the Chair for IEEE AP-S Technical Committee on Antenna Measurement from 2018 to 2020. He is a Distinguished Lecturer for IEEE Antennas and Propagation Society from 2022 to 2024. He is a Fellow of the Singapore Academy of Engineering.

CHAU YUEN (Fellow, IEEE) received the B.Eng. and Ph.D. degrees from Nanyang Technological University, Singapore, in 2000 and 2004, respectively.

He was a Postdoctoral Fellow with Lucent Technologies Bell Labs, Murray Hill, in 2005. From 2006 to 2010, he was with the Institute for Infocomm Research, Singapore. From 2010 to 2023, he was with the Engineering Product Development Pillar, Singapore University of Technology and Design. Since 2023, he has been with the School of Electrical and Electronic Engineering, Nanyang Technological University. He is Currently a Provost's Chair of Wireless Communications, and the Assistant Dean of Graduate College. He has four U.S. patents and published over 400 research papers at international journals.

Dr. Yuen received the IEEE Communications Society Leonard G. Abraham Prize in 2024, the IEEE Communications Society Best Tutorial Paper Award in 2024, the IEEE Communications Society Fred W. Ellersick Prize in 2023, the IEEE Marconi Prize Paper Award in Wireless Communications in 2021, the IEEE APB Outstanding Paper Award in 2023, and the EURASIP Best Paper Award for Journal on Wireless Communications and Networking in 2021. He currently serves as an Editor-in-Chief for *Nature Computer Science* (Springer), an Editor for IEEE Transactions on Vehicular Technology, IEEE SYSTEM JOURNAL, IEEE TRANSACTIONS ON NETWORK SCIENCE AND ENGINEERING, where he was awarded as IEEE TNSE Excellent Editor Award, and a Top Associate Editor for IEEE TRANSACTIONS ON VEHICULAR TECHNOLOGY from 2009 to 2015. He also served as a Guest Editor for several special issues, including IEEE JOURNAL ON SELECTED AREAS IN COMMUNICATIONS, *IEEE Wireless Communications Magazine*, *IEEE Communications Magazine*, *IEEE Vehicular Technology Magazine*, IEEE TRANSACTIONS ON COGNITIVE COMMUNICATIONS AND NETWORKING, and *Applied Energy* (Elsevier). He is a Distinguished Lecturer of IEEE Vehicular Technology Society, Top 2% Scientists by Stanford University, and also a Highly Cited Researcher by Clarivate Web of Science.